7

Application of the Particle Image Velocimetry to the Couette-Taylor Flow

Innocent Mutabazi[1], Nizar Abcha[2],
Olivier Crumeyrolle[1] and Alexander Ezersky[2]
[1]*LOMC, UMR 6294, CNRS-Université du Havre 53, rue Prony, Le Havre Cedex,*
[2]*M2C, UMR 6143, CNRS-University of Caen-Basse Normandie,*
France

1. Introduction

For longtime, the investigation of flow regimes has been achieved using fluorescent particles or anisotropic reflective particles. Fluorescent particles are suitable for open flows (Van Dyke, 1982) such as flows in channels (Peerhossaini *et al.*, 1988) or flows behind a cylinder (to visualize Benard-von Karman street) (Provansal *et al.*, 1986; Mutabazi *et al.*, 2006). For closed flows such as flows in a rectangular cavity or in an annular cylindrical rotating cavity, fluorescent particles rapidly color the entire flow and no flow structure can be caught. Anisotropic reflective particles (aluminium, iriodin or Kalliroscope flakes) are more convenient for detection of the flow structures (Taylor, 1923; Andereck *et al.*, 1986; Coles, 1965; Matisse *et al.*, 1984; Dominguez-Lerma *et al.* , 1985; Thoroddsen *et al.* 1999). A laser light is used to illuminate the flow cross-sections and to detect the flow structure in the axial, radial and azimuthal directions. The motion of the seeded particles in a fluid gives a qualitative picture of flows which can be used to develop appropriate theoretical models. The development of chaotic models of fluid flows (Rayleigh-Bénard convection, Couette-Taylor flow or plane Couette flow) has benefited from observations using visualizations techniques (Bergé *et al.*, 1994). Using appropriate signal processing techniques such as space-time diagrams and complex demodulation, it is possible to obtain spatio-temporal evolution of the flows (Bot *et al.*, 2000). In order to obtain quantitative data on velocity fields, different velocimetry techniques have been developed such as Laser Doppler Velocimetry (LDV, Durst *et al.*, 1976, Jensen 2004), Ultrasound Doppler Velocimetry (UDV, Takeda *et al.*, 1994) and Particle Image Velocimetry (PIV, Jensen, 2004). Nowadays, there is a lot of literature on velocimetry techniques the development of which is beyond the scope of this chapter, some of them and their applications are described in this volume. Each velocimetry technique has its advantages and own limitations depending on the flow system under consideration. For example, in the case of the Couette-Taylor flow, the LDV (Ahlers *et al.*, 1986) gives time averaged velocity in a point, the UDV measures a velocity profile along a chosen line in the flow and the PIV gives a velocity field in a limited flow cross section. The Couette-Taylor system is composed of a flow in the gap between two coaxial differential rotating cylinders. This system represents a good hydrodynamic prototype for the study of the transition to turbulence in closed systems. The experimental results obtained from this system have led

to the development of powerful theoretical models for the transition to chaos (Chossat *et al* . (1994)). Beside the theoretical interpretation of patterns observed in the Couette-Taylor system, many theoretical attempts have been made to connect flow quantitative properties and visualized structures by anisotropic particles (Matisse *et al*. , 1984; Savas (1985), Gauthier *et al*., (1998)). The application of PIV in the Couette-Taylor system with a fixed outer cylinder was first performed by Wereley & Lueptow (Wereley *et al*., 1994, 1998) followed later by few authors. The question of correlation between velocimetry data and qualitative structure given by anisotropic reflective particles in the Couette-Taylor flow was addressed only recently (Gauthier *et al*., 1998; Abcha *et al*., 2008). However, many questions connected with the interpretation of results obtained by different techniques have not been answered. A special attention is paid to some of these unresolved problems.

This chapter illustrates how the PIV technique can be applied to the Couette -Taylor system. Two special cases are described: 1) flow patterns obtained when the outer cylinder is fixed while the inner is rotating; 2) flow patterns achieved when both cylinders are in contra-rotation. A detailed comparison between PIV and visualisation by anisotropic reflective particles will be provided for illustration of the complementarity between these two techniques. The chapter is organized as follows. The experimental setup and procedure are presented in the next section. Section 3 is devoted to the flow visualization by Kalliroscope particles and the space-time diagram technique. In section 4, the description of PIV and its adaptation to the Couette-Taylor flow are described. Section 5 contains results for flow regimes when the outer cylinder is fixed (Taylor Vortex Flow (TVF) and Wavy Vortex Flow (WVF)). Section 6 gives results for spiral vortex flow when both cylinders are sufficiently counter-rotating. Section 7 summarizes the content of the chapter.

List of symbols

a	Inner cylinder radius, cm
b	Outer cylinder radius, cm
d	Size gap, cm
g	Gravity acceleration
L	Cylinder length, cm
Re	Reynolds number
Ta	Taylor number
n	Optical refraction index
vs	Sedimentation velocity
V_r	Radial velocity component, m/s
u	Dimensionless radial velocity
V_z	Axial velocity component, m/s
w	Dimensionless axial velocity
Δt_{res}	Residence time, s
Abs	Absolute value
CCF	Circular Couette Flow
TVF	Taylor Vortex Flow
WVF	Wavy Vortex Flow
MWVF	Modulated Wavy Vortex Flow
TTVF	Turbulent Taylor Vortex Flow
SVF	Spiral Vortex Flow

OC Outer cylinder
IC Inner cylinder
Γ Aspect ratio
η Radius ratio
Ω Angular velocity, rad/s
ξ Dimensionless radial coordinate
ζ Dimensionless axial coordinate
ν Kinematic viscosity, m^2/s
ρ Fluid density, g/cm^3
λ Pattern wavelength

2. Experimental apparatus

The experimental system consists of two vertical coaxial cylinders, immersed in a large square Plexiglas box filled with water in order to maintain a controlled temperature (Fig. 1). The square box allows to minimize distortion effects of refraction due to curvature of the outer cylinder during optical measurements. The inner cylinder made of aluminium has a radius a = 4 cm, the outer cylinder made of glass has a radius b = 5 cm, the gap between the cylinders is $d = b\text{-}a$ = 1 cm and the working height is L = 45.9 cm. Therefore the radius ratio $\eta = a/b$ = 0.8 and the aspect ratio is $\Gamma = L/d$ = 45.9. Such an aspect ratio is large enough to avoid the end effects; the flow system is considered as an extended system. The gap is filled with a deionized water for which $\nu = 9.8.10^{-3} cm^2/s$ at the temperature T = 21.2°C. Its size has been chosen in order to obtain a good resolution in the radial direction.

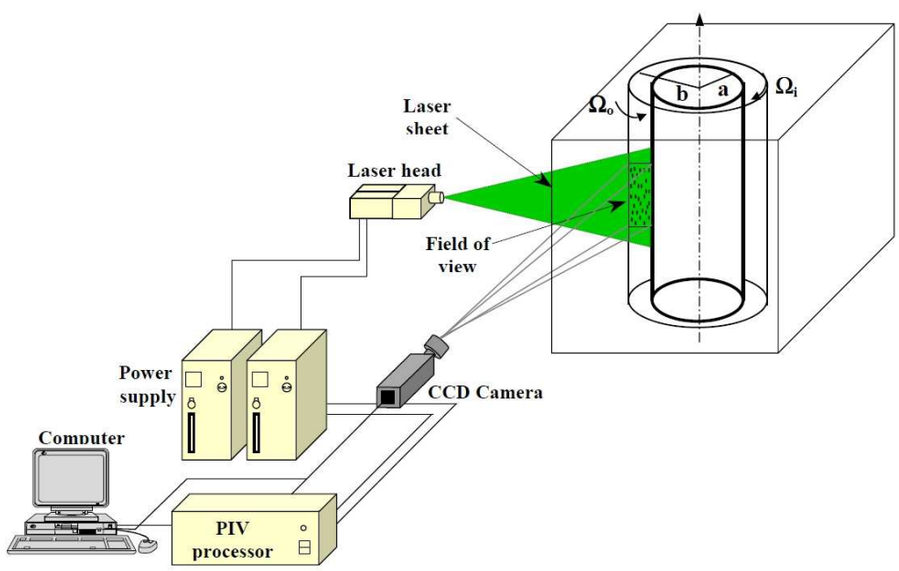

Fig. 1. Experimental apparatus: scheme of visualization and data acquisition system

The cylinders are rotated by two servomotors at controlled angular rotation frequencies Ω_i and Ω_o. The control parameters are the Reynolds numbers defined for each cylinder : $Re_i = \Omega_i ad/\nu$ and $Re_o = \Omega_o bd/\nu$ for the inner and outer cylinder respectively. When $Re_0 = 0$, the Taylor number is often preferred: $Ta = Re_i (d/a)^{1/2}$. Three cameras have been implemented on

the experimental table: a linear CCD camera of 1024 pixels that records the light reflected by anisotropic reflective particles along a line parallel to cylinder axis. The second camera is a 2-d IEEE1394 camera (A641f, Basler) that is used to record the flow motion in the (r,z) plane; this record allows a better investigation of the flow in the radial direction. The third camera is a CCD camera (Kodak) with 1034x779 pixels for PIV data recording. All cameras were connected to a computer for data recording and processing.

3. Visualization by Kalliroscope particles and space-time diagrams

Particles added to the flow must have controlled characteristics such as size, distribution, and concentration. These particles must be small enough to be good flow tracers and large enough to scatter sufficient light for imaging. In the Couette-Taylor flow, the commonly used particles are Kalliroscope flakes of typical size of 30 µm x 6 µm x 0.07 µm (Matisse *et al*. 1984) with a relatively large reflective optical index $n = 1.85$ and a density of $\rho' = 1.62$ g/cm^3. A concentration of 1% to 2% reflective particles is added to water to realize a Kalliroscope AQ1000 suspension, 2% per volume of which was added to the working solution. The sedimentation of these particles remains negligible in horizontal or vertical configurations if the experiment lasts less than 10 hours (Matisse *et al*., 1984) because their sedimentation velocity is $v_s = 2\ a^2 g(\rho'-\rho)/(9\nu\rho) = 2.8\ 10^{-5}$cm/s. The time scales related to the particle motions (transient, rotation and diffusion) were discussed in detail by Gauthier *et al.* (1998). These particles do not modify significantly the flow viscosity and no non-Newtonian effect was detected as far as small concentrations ($c < 5\%$) are used (Dominguez-Lerma *et al*., 1985). The choice of the concentration of 2% was done to ensure the best contrast in the flow. The values of the control parameters (Re_o, Re_i) were determined within a precision of 2%.

Increasing values of the control parameters leads to the occurrence of different patterns in the Couette-Taylor flow depending of whether both cylinders rotate or only the inner cylinder is rotating (Fig. 2, 3). A whole state diagram of flow regimes in the Couette-Taylor system has been established by Andereck (Andereck *et al*., 1986) for a configuration with radius ratio $\eta = 0.883$ and aspect ratios Γ ranging from 20 to 48. When the outer cylinder is fixed and the inner Reynolds number Re_i is increased, the transition sequence is the following : Circular Couette Flow (CCF) bifurcates to Taylor Vortex Flow (TVF) which is formed of axisymmetric stationary vortices, then to Wavy Vortex Flow (WVF) oscillating in the azimuthal and axial directions with a frequency f and an azimuthal wavenumber m; the later bifurcates to Modulated Wavy Vortex Flow (MWVF) characterized by two incommensurate frequencies. The ultimate state is the Turbulent Taylor Vortex Flow (TTVF) iin which large scale vortices of the size of the gap and small vortices of different scales coexist. In case of counter-rotating cylinders, the bifurcation of the circular Couette flow leads to spiral vortex flow (SVF) composed of helical vortices travelling in axial and azimuthal directions, followed by interpenetrating spirals then by wavy spirals and modulated waves before transition to turbulence. Interpenetrating spirals, wavy spirals and modulated waves are characterized by incommensurate frequencies. Using a He-Ne Laser sheet (whose wavelength is 632 nm, one millimetre wide beam, spread by a cylindrical lens), it was possible to visualize the cross section of the flow in the r-z plane. Fig. 3 gives the cross section of regimes observed in the Couette-Taylor system for different values of the control parameters. Linear CCD camera of 1024 pixels was used to record a reflected light intensity $I(z)$. Records were performed at regular time intervals along a line in the centre of the flow

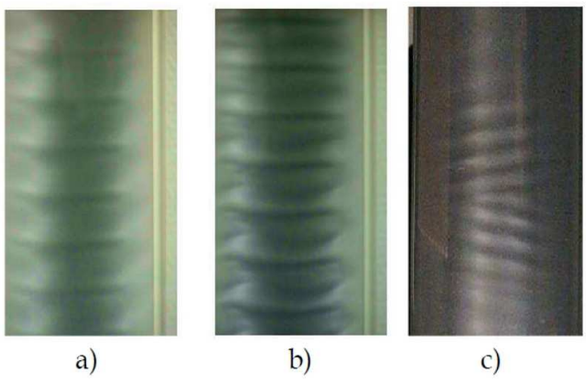

Fig. 2. Pictures of flow regimes in the Couette-Taylor system : a) TVF, b) WVF, c) SVF with a sink.

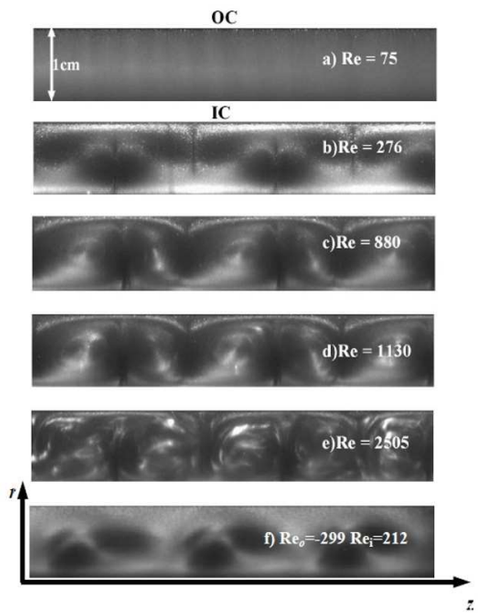

Fig. 3. Cross-section of : a) CCF, b) TVF, c) WVF, d) MWVF, e) TTVF, f) SVF. OC and IC stand for outer and inner cylinder respectively.

cross-section (r = a + d/2), parallel to the cylindrical axis over a length of 27.8 cm in the central part of the flow system. The intensity was sampled over a linear range of 256 values, displayed in gray levels at regular time intervals in order to produce space-time diagrams $I(z,t)$ of the pattern which exhibits the temporal and spatial evolution of vortices (Fig. 4a). The radial variation of intensity $I(r)$ was recorded using a 2-d IEEE1394 camera, and then sampled at regular time intervals to obtain the space-time diagram $I(r,t)$. Examples are illustrated (Fig. 4) for wavy vortex flow and in Figure 5 for spiral vortex flow.

A cross-section of spiral vortex flow is shown in Fig. 5-a; its space-time diagram in the axial and radial directions are shown respectively in Fig. 5-b and Fig. 6. The right and left travelling spirals merge into a single point called "sink" at $z = z_0$ (Fig. 5-a). Using a 2-D Fast Fourier Transform (FFT), it is possible to obtain the axial wavenumbers and the frequencies

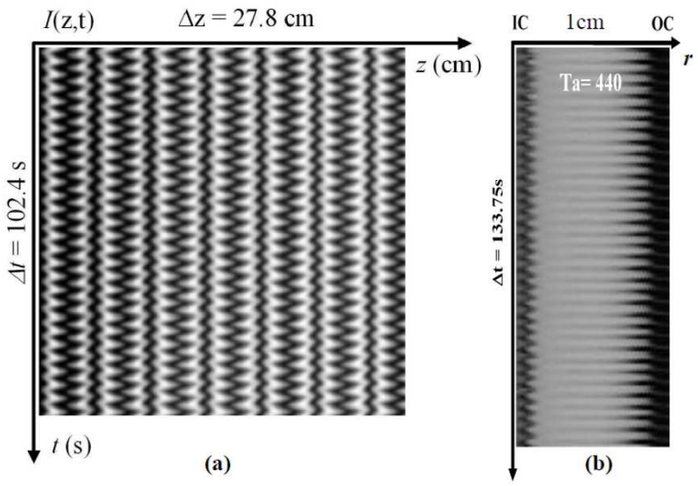

Fig. 4. Space-time diagrams for Wavy Vortex Flow (Re_o = 0; Re_i = 880) cross section of which is shown in Fig. 2 : (a) axial distribution *I(z,t)*; (b) radial distribution *I(r,t)*.

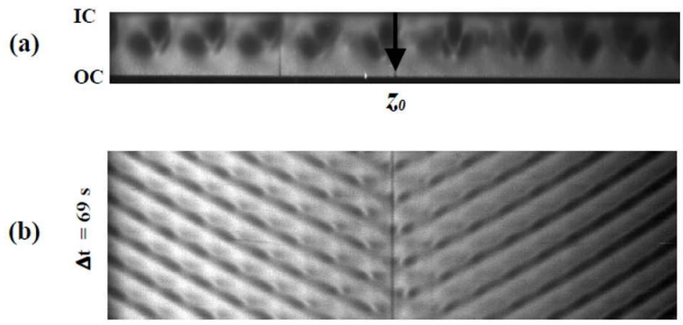

Fig. 5. Spiral pattern for Re_o = - 230 and Re_i = 174 just above the critical value (Re_{ic} = 160, ε = 0.0875): (a) cross-section of flow; (b) space- time diagrams *I(z,t)* taken in the mid-gap position (x = 0.5) over the axial length Δz = 13.8 cm

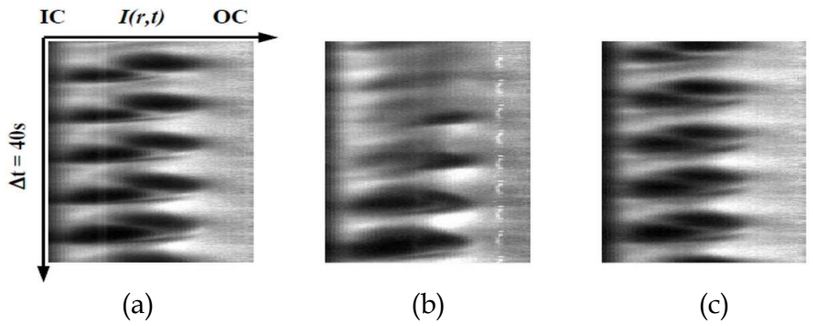

Fig. 6. Space- time diagrams *I(r,t)* of the spiral pattern : (a) before the sink; (b) in the sink; (c) after the sink.

of oscillations of the patterns. The FFT can be complemented by the complex demodulation technique (Bot *et al.* 2000) in order to determine the physical properties like phase, amplitude, frequency, and wavenumber of more complex patterns (in the presence of localized defects, sinks or sources) . These techniques were applied to the spiral pattern of

Figure 5-b. Analysis of temporal and spatial spectra show that the left and right spirals have different frequencies and wavenumbers: f_R = 0.166 Hz ≠ f_L = 0.163 Hz and k_R = 5.21 cm^{-1} ≠ k_L = 5.06 cm^{-1}. The standard deviations on measured frequencies and wavenumbers are Δf = ± 0.002 Hz and Δk = ± 0.04 cm^{-1} respectively.

The azimuthal wavenumber of the spiral flow can be determined by measuring the inclination angle θ of the spirals and extracting the value of m from the formula $\theta = \arctan(m\lambda/(2\pi R)) = \arctan(m/(kR))$ where λ is the wavelength and R = (a+b)/2 is the mean radius. For Re_o= -230 and Re_i = 174 the obtained values are m = 2 and θ = 4.88° while for Re_o= -251 and Re_i = 202: m = 2 and θ = 4.85°. Therefore, the space-time diagrams of the spiral pattern in Figure 4 can be represented by the following signal [Cross *et al.*, 1993]:

$$I(r,z,t) = F(r)\left\{ \mathrm{Re}[A(z,t)e^{i\left(\omega_R t - k_R z\right)} + B(z,t)e^{i\left(\omega_L t + k_L z\right)}]e^{-im\theta} \right\} \tag{1}$$

where A and B are the amplitudes of right-handed and left-handed spirals respectively, ω_R = $2\pi f_R$, ω_L = $2\pi f_L$ are the corresponding frequencies, k_R and k_L the corresponding axial wavenumbers, m their azimuthal wavenumber and c.c. stands for complex conjugate. The "structure function" $F(r)$ characterizes the radial dependence of the spiral pattern and vanishes at the cylindrical surfaces: $F(r = a) = F(r = b) = 0$ (Fig. 7). The amplitudes $A(z,t)$ and $B(z,t)$ satisfy the complex Ginzburg-Landau equations (Cross *et al.*, 1993):

$$\tau_0\left(\frac{\partial A}{\partial t} + s\frac{\partial A}{\partial z}\right) = \varepsilon(1+ic_0)A + \xi_0^2(1+ic_1)\frac{\partial^2 A}{\partial z^2} - g(1+ic_2)|A|^2 A - \delta(1+ic_3)|B|^2 A \tag{2a}$$

$$\tau_0\left(\frac{\partial B}{\partial t} - s\frac{\partial B}{\partial z}\right) = \varepsilon(1+ic_0)B + \xi_0^2(1+ic_1)\frac{\partial^2 B}{\partial z^2} - g(1+ic_2)|B|^2 B - \delta(1+ic_3)|A|^2 B \tag{2b}$$

where τ_0, ξ_0 represent the characteristic time and characteristic length of perturbations, s their group velocity, ε is the criticality, g the Landau constant of nonlinear saturation, δ is the coupling constant of left and right travelling spirals, c_i are the dispersion coefficients. These coefficients can be determined either numerically (Demay *et al.* , 1984; Tagg *et al.* 1990) or experimentally (Goharzadeh *et al.*, 2010); their values depend on the control parameters

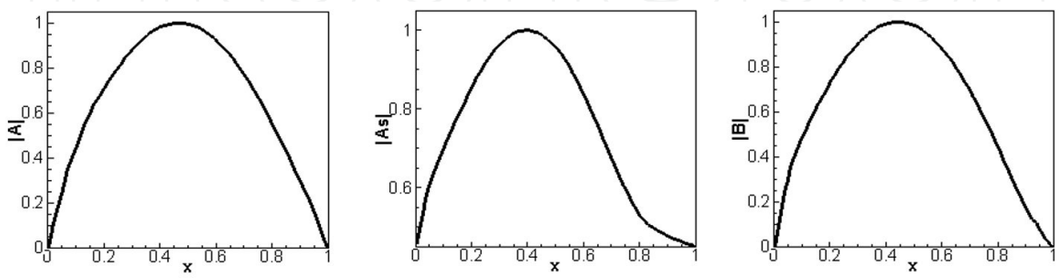

(a) (b) (c)

Fig. 7. Structure function $F(r)$ of the time-averaged amplitude of the pattern $I(r,t)$ for Re_o = -230 and Re_i = 174: (a) before the sink; (b) in the sink; (c) after the sink.

Re_i and Re_o. The patterns shown in Fig. 5 and time-averaged amplitude profiles of which are shown in Fig. 8 correspond to the case when $\delta > 1$, i.e. the wave coupling is destructive. The sink corresponds to the intersection of two amplitudes solutions given by $A(z) = B(z)$.

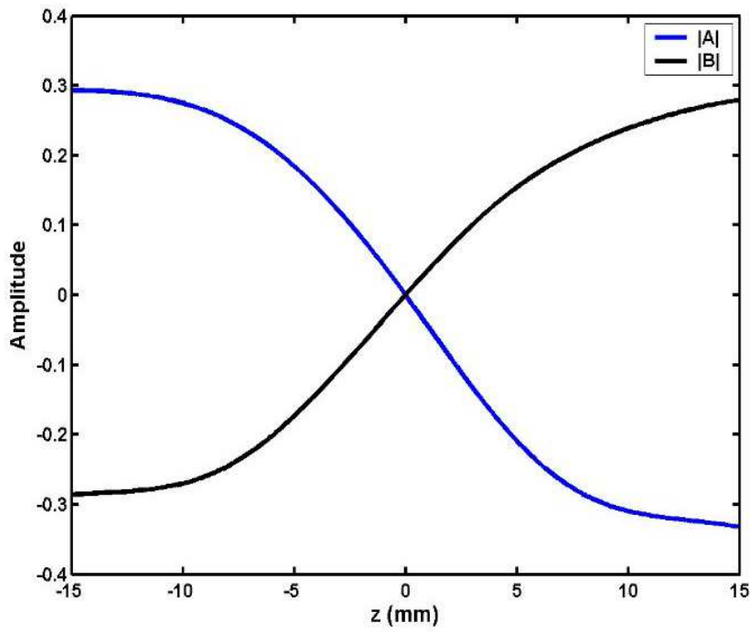

Fig. 8. Spatial distribution of the time-averaged amplitude of the right and left spiral, for Re_o = -230 and Re_i = 174 in the neighbourhood of the sink localized in z_0 = 64 mm.

The fit of experimental data with the theoretical curves (Fig.8) $A(z) = A_0 \tanh[(z - z_0)/\xi]$ and $B(z) = A_0 \tanh[-(z - z_0)/\xi]$ gives A_0 = 0.3, ξ = 7.14 mm = 0.714 d. The value of the coefficient ξ_0 in the equations (2) is given by $\xi_0 = \xi \varepsilon^{1/2} = 2{,}11$ mm. This value is in a good agreement with theoretical values $\xi_0/d \approx 0.2$ (Tagg *et al.*, 1990]. The structure functions in Fig. 7 show that the source weakly affect the radial flow.

4. Description of the PIV and its adaptation to the Couette-Taylor flow

The technique of space-time diagrams does not provide quantitative data on the velocity or vorticity fields that are important for the estimate of energy or momentum transfer in the different regimes. Thus it is necessary to perform particle image velocimetry in order to get more quantitative data. For PIV measurements, the working fluid was seeded with spherical glass particles of diameter 8-11 μm and density ρ = 1.6 g/cm^3, with a concentration of about 1ppm. The diffusion time of such particles is $\tau_D = 3\pi\rho\nu d_p^3 / 4k_B T \approx 500\ s$ where d_p is the particle diameter. The particle Reynolds number $Re_p = Ud_p/\nu < 0.1$ or equivalently their Stokes number $St = (\rho_p d_p/\rho d)Re_p < 10^{-3}$ so that they are assumed to follow the flow streamlines, i.e. they are good tracers of the flow. Here U is the characteristic velocity of the particle. The PIV system consists of two Nd-

YAG Laser sources, a MasterPiv processor (from Tecflow) and a CCD camera (Kodak) with 1034x779 pixels. The time delay between two Laser pulses varies from 0.5 to 25 ms, depending on the values of Reynolds numbers Re_i and Re_o. The flow in the test area of the plane (r,z) is visualized with a thin light sheet that illuminates the glass particles, the positions of which can be recorded at short time intervals. To obtain velocity field, 195 pairs of images of size 1034 x 779 pixels were recorded. Each image of a pair was sampled into windows of 32x32 pixels^2 with a recovering of 50%. The velocity fields were computed using the intercorrelation function, which is implemented in the software "Corelia-V2IP" (Tecflow). The PIV measurements were performed in the CCF, in the TVF and WVF regimes in order to calibrate our data acquisition system and to fit data available in the literature for these regimes (Wereley *et al*. 1994, Wereley *et al*. 1998, Abcha *et al*. 2008).

In the circular Couette flow, the spherical glass particles are uniformly distributed (Fig. 9a) while in the TVF and WVF, after 10 hours, the particles have migrated towards the vortex cores where the radial velocity vanishes (Fig. 9b). The PIV allows to visualize velocity and vorticity fields in the cross section (r,z). The results of the complete process is illustrated by 2D velocity fields of Fig. 10a, b. The inflow (arrow (2)) and outflow (arrow (3)) are clearly evidenced in the case of the TVF and WVF. The measured radial and axial velocity components $V_r(r)$, $V_z(r)$ at a given axial position z or at a given radial position r are plotted in Fig. 10c-h in scaled units.

The radial and axial velocity components have been fitted by a polynomial function satisfying the non-slip condition at the cylindrical walls $r = a$ and $r = b$. The velocity data are scaled by the inner cylinder velocity $a\Omega_i$ as follows : $u = V_r/a\Omega_i$ $w = V_z/a\Omega_i$. The lengths are scaled by the gap size, the radial position becomes $\xi = (r - a)/d$ and the axial coordinate is $\zeta = z/d$. In order to plot their profiles, time-averaged velocity components were computed in the axial and radial directions (Fig.10). The instantaneous velocity components can be superposed chronologically at regular time intervals in order to obtain space-time diagrams in both direction (z,t) and (r,t) (Fig. 11). The resulting diagrams are colour-coded as in Abcha *et al*. 2008.

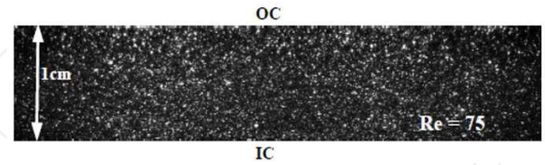

(a)

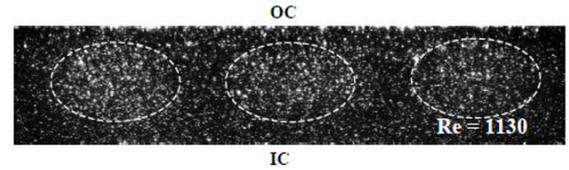

(b)

Fig. 9. Cross section of flow visualized with glass particles for: a) the CCF (Ta = 37.5), b) the WVF (Ta = 565).

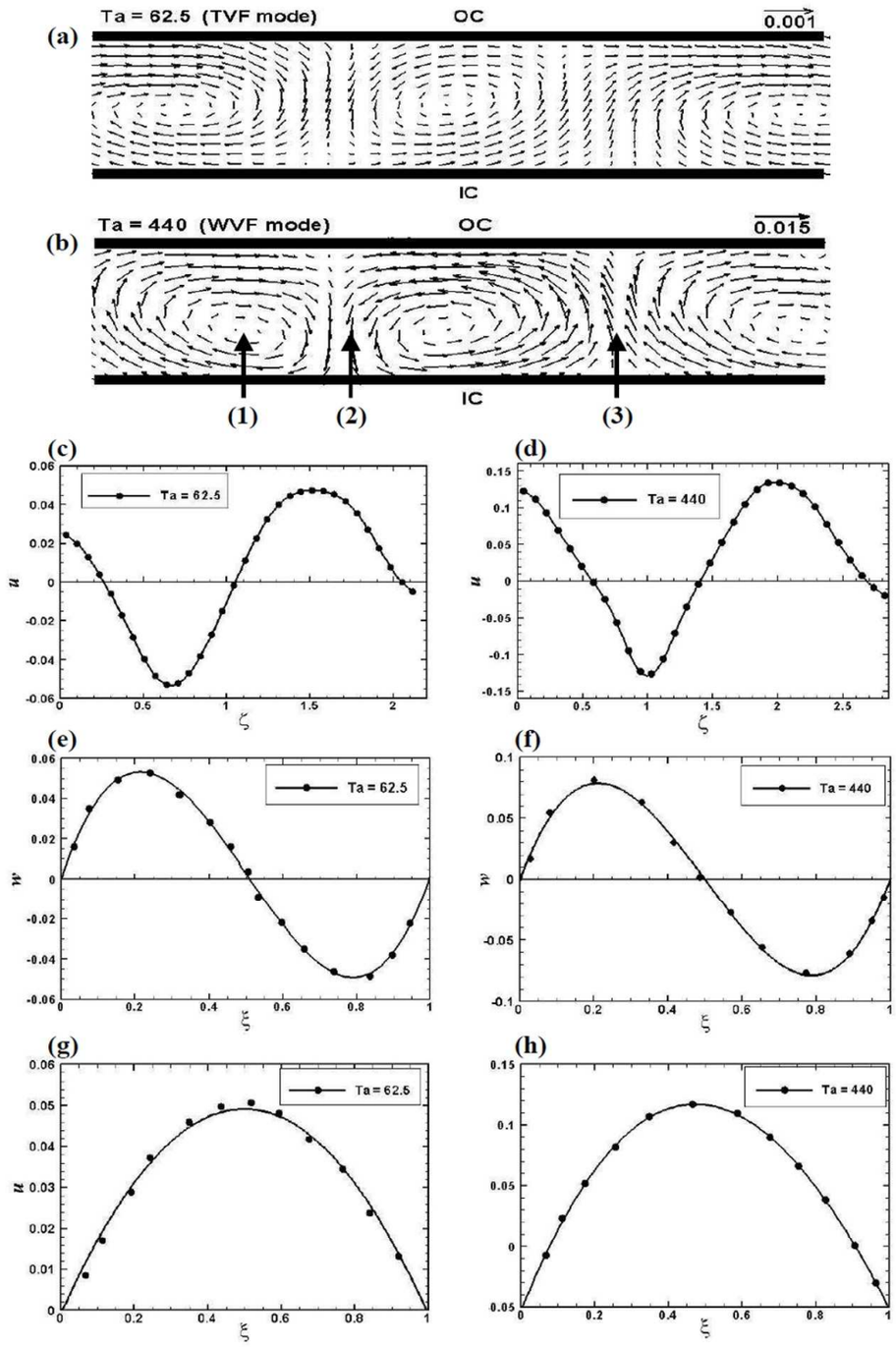

Fig. 10. a); b) Velocity field from PIV measurement; c-d) axial variation of velocity component $u(\zeta)$ at the midgap ($\xi = 0.5$). Radial variation of velocity components: e-f) axial component $w(\xi)$ in the vortex core (arrow (1)): and g-h) radial component $u(\xi)$ at outflow (arrow (3)) for TVF (Ta = 62.5), WVF (Ta = 440) .

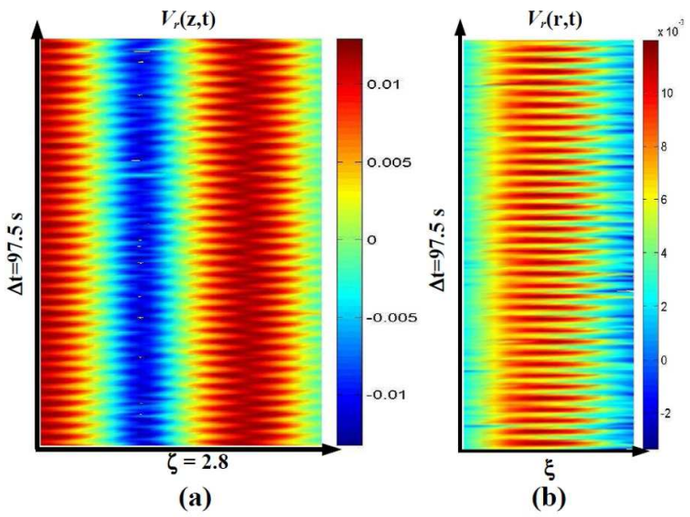

Fig. 11. Space-time diagrams for Ta = 440: a) $V_r(z,t)$ taken at the midgap x = 0.5, b) $V_r(r,t)$ at outflow position. The red colour corresponds to positive values and blue to negative values of the velocity.

5. Spatio-temporal structure of Taylor vortex flow and wavy vortex flow

5.1 Velocity fields

The instantaneous velocity fields of the Taylor vortex flow in the radial-axial plane, just above the transition to supercritical flow at Re_i = 125 for 4 records (t_{i+1}= t_i+0.5s) are shown in Fig. 12. These velocity fields illustrate the dynamics of the TVF: a regime composed of stationary counter-rotating vortices characterized by spatial periodicity equal to twice the size of the gap. The traditional flow visualization of wavy vortex flow by observing the motion of small particles at the outer cylinder suggests that the vortices passing a point on

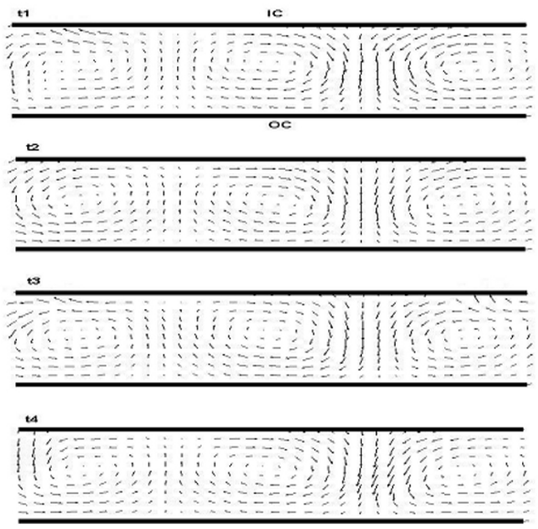

Fig. 12. Instantaneous velocity fields of TVF at Re_i =125 for 4 records (t_{i+1}=t_i+0.5s).

the outer cylinder oscillate axially. The PIV permits to visualize the significant transfer of fluid between adjacent vortices in the time and to check the time-dependent theory of shift-and-reflective symmetry in the vortex using the models of wavy vortex flow (Marcus *et al.* 1984). Although the axial motion of the vortices is evidently based on the location of the vortex centres, marked by diamonds (Fig.13), the significant transfer of fluid between adjacent vortices indicates that vortex cells are not independent. The transfer of fluid occurs in a cyclic fashion with a particular vortex gaining fluid from adjacent vortices and then losing fluid to adjacent vortices.

The cycle can be described most easily with reference to the center vortex of « vortex 0 » in Fig. 13. The cycle begins by the frame (i) and ends by the frame (vii). During the cycle the fluid moves from the inner part of the left-hand vortex flowing into the middle vortex and toward the outer cylinder. Simultaneously, fluid from the center vortex moves into the right-hand vortex and toward the inner cylinder. The flow out of the right-hand side of the middle vortex shifts as it is shown in frame (iii), so that now the middle vortex is gaining fluid from the left-hand vortex without losing any fluid. An inward flow from the right-hand vortex also feeds fluid into the middle vortex (see frame (iv)). Frames from (v) to (vii) demonstrate the reversed process beginning with flow around the inner side of the middle vortex from right to left, followed by flow out of the middle vortex to the left, then flow out

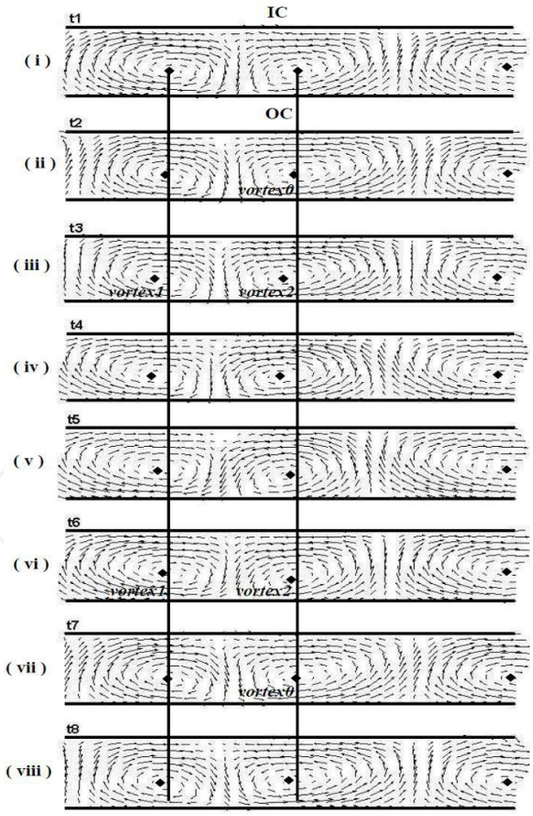

Fig. 13. The instantaneous velocity fields of WVF at Re_i = 880 for 8 records ($t_{i+1}=t_i+0.5s$), the time progresses from top to bottom through one complete cycle of an azimuthal wave passing the measurement plane

to the left and right, and finally to the right only. These observations led to the conclusion that the middle vortex is losing the same amount of fluid during the second half of the cycle as it gained in the first half. The second half of the cycle (frames (v)-(vii)) appears identical to the first half of the cycle (frames (i)-(iv)) by a rule of reflective symmetry. For example, the vortex 2 in the field (vi) is a reflection of vortex 1 in the field (iii) with reversal of flow direction, that is to say that the flow of the left vortex from to the middle of the field (iii) became the flow of the middle vortex to the left the vortex of field (vi). This is called ''shift-and-reflect'' symmetry (Marcus, 1984).

5.2 Other hydrodynamic fields

From velocity fields (Fig. 12, 13), different quantities of the flow perturbations in the cross section (*r*,*z*) can be computed for each regime (Fig. 14):

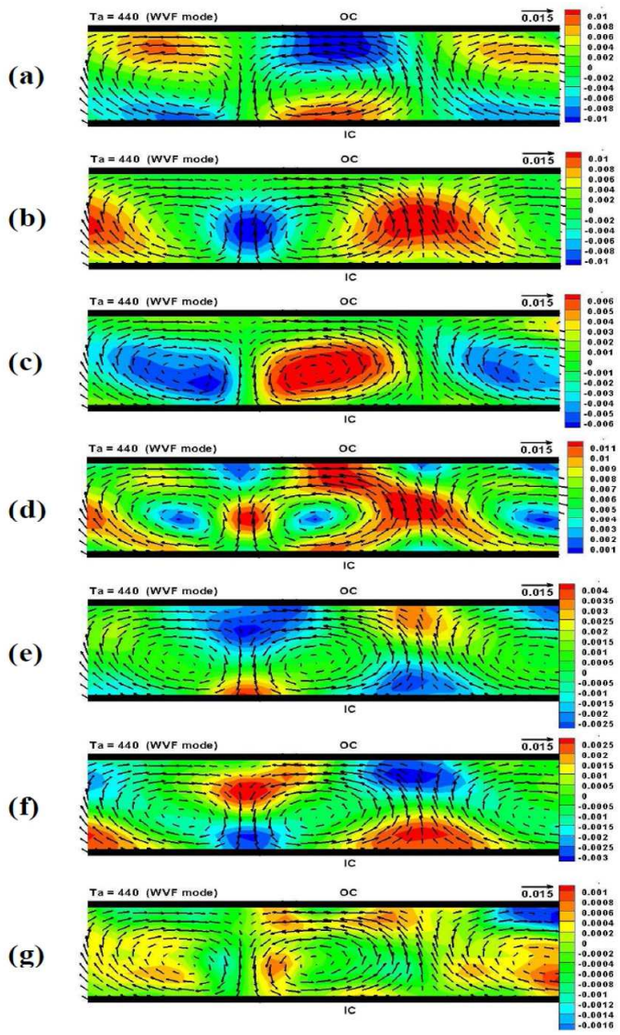

Fig. 14. Cross-section (*r*,*z*) of hydrodynamics fields for WVF on the background of vector velocity field: a) Axial velocity; b) radial velocity; c) vorticity; d) kinetic energy; e) axial elongation; f) radial elongation; g) shear rate.

- the azimuthal vorticity component ω_θ and the kinetic energy E:

$$\omega_\theta = \left(\partial V_r / \partial z - \partial V_z / \partial r\right) \; ; \; E = (V_r^2 + V_z^2)/2 \tag{3}$$

- three components of the shear rate tensor:

$$\dot{\varepsilon}_{rr} = \partial V_r / \partial r \; ; \; \dot{\varepsilon}_{zz} = \partial V_z / \partial z \; ; \; \dot{\varepsilon}_{rz} = \left(\partial V_r / \partial z + \partial V_z / \partial r\right)/2 \tag{4}$$

The vorticity fields and velocity components show that inflow and outflow are almost symmetric in the Taylor vortex flow (Fig. 10a 10c) while they are dissymmetric in the wavy vortex flow (Fig. 10b 10d) because of the oscillations of the separatrix.

5.3 Space-time dependence of velocity profiles

In order to have the most complete information on dynamics of vector velocity field, records of instantaneous profiles of both axial and radial velocity components were superimposed chronologically at regular time intervals (Fig. 15, 16) with color code as in Figure 11. For example, Fig. 15 illustrates the space-time diagram of radial $V_r(z,t)$ and axial velocity $V_z(z,t)$ of TVF (Re_i = 125). The red colour corresponds to the outflow and the blue colour to the inflow. In Fig. 16, the space-time diagram of radial $V_r(r,t)$ and axial velocity $V_z(r,t)$ of WVF (Re_i = 880), were the red colour corresponds to anti-clockwise vortex core and the blue colour to clockwise vortex core.

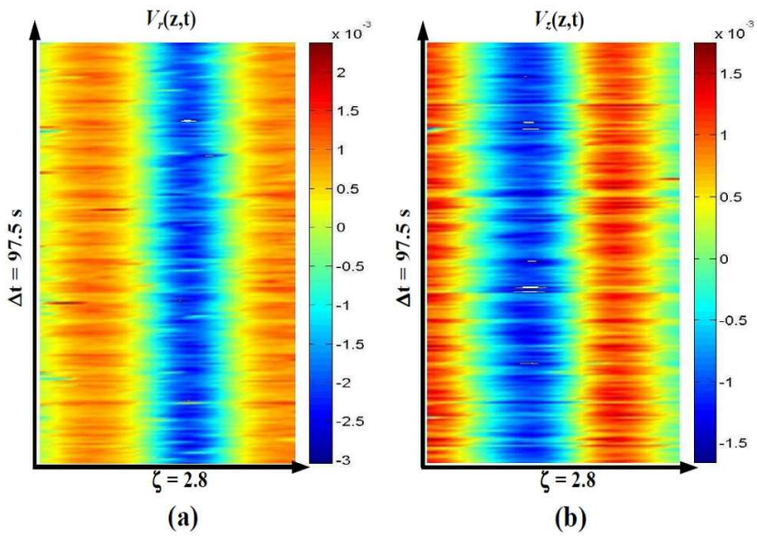

Fig. 15. Space-time diagrams of velocity components for TVF (Re_i=125): a) V_r(z,t) maeasured at the midgap ξ = 0.5 and b) V_z(z,t) near the outer cylinder at ξ = 0.75.

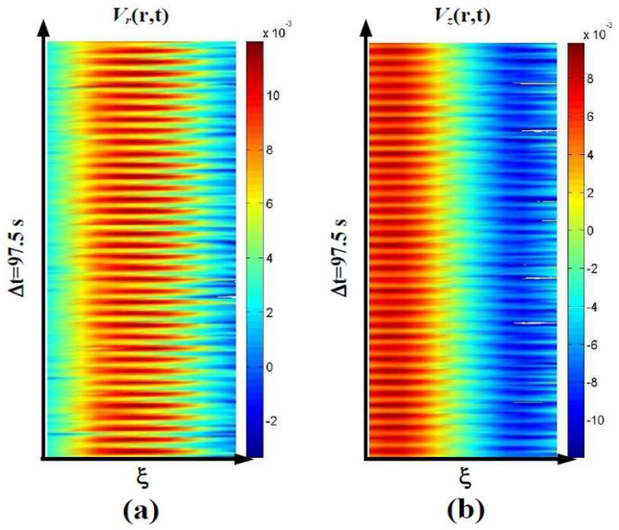

Fig. 16. Space-time diagrams for WVF (Re_i = 880): (a) V_r(r,t) at outflow position, (b) $V_z(r,t)$ in the core of anticlockwise vortex.

5.4 Intensity of light reflected by Kalliroscope *vs*. velocity component

Fig. 17a and Fig. 18a compare the space-time diagrams obtained from PIV measurements (Fig. 11) with those obtained from flow visualization by Kalliroscope flakes in both directions for a wavy vortex regime at Re_i = 880. Unlike space time diagrams of velocities components, space-time diagrams obtained from the reflected light intensity do not give any information about the flow direction (upward or downward for $I(z,t)$, inward vs. outward for $I(r,t)$). That is why for comparison, the absolute values of the velocity components obtained by PIV are used.

At first glance, it was realized that the space-time diagrams obtained by Kalliroscope flakes are very similar with those of the radial velocity component $V_r(z,t)$ and $V_r(r,t)$. Fig. 17b and Fig. 18b illustrate the time-average profiles in the axial and radial directions. These plots highlight the fact that Kalliroscope particles give a signature of the radial velocity component measured in the centre of the gap (ξ = 0.5). The minima and maxima are reached for identical axial positions. A similar correspondence is obtained with the envelopes of the space-time diagrams in the axial and radial directions and leads to the same conclusion (Fig. 17b and Fig. 18b): a perfectly identical evolution in the annular space, a maximum reached in the middle of the gap and minima at the walls of two cylinders. Moreover, the absolute value of the radial velocity vanishes in the vortex core while it reaches the maximum in the outflow and in the inflow. The reflected light intensity vanishes in the vortex core because of the weak motion of Kalliroscope flakes. In the inflow and outflow where the Kalliroscope flakes are faster in the radial direction, the intensity is much larger than in the other parts of the flow.

Recent numerical simulations (Gauthier *et al*. 1998) have shown that the Kalliroscope or iriodin particles may be related to the radial velocity component but no measurements were provided to sustain these arguments. The relaxation time τ of the Kalliroscope flakes is about 0.01 T_p, where the precession time $T_p \sim d/V_r \sim d/V_z \approx$ 2s for the TVF and $T_p \approx$ 1s for WVF. The time scale of the Brownian orientation in a water flow is about 100 s at room temperature (Savas, 1985); it is large enough compared to other time scales of our experiment

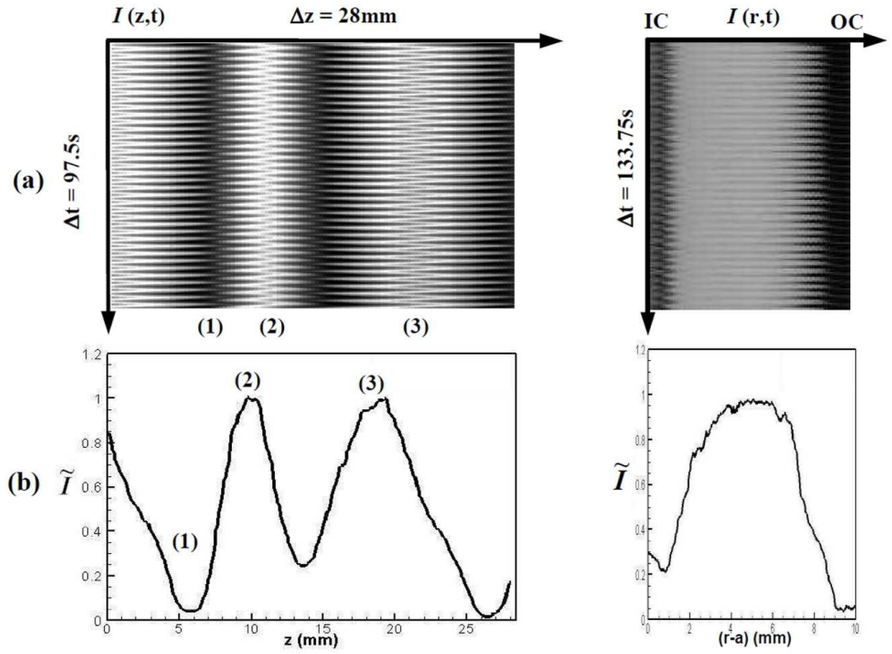

Fig. 17. a) Space-time diagrams of the intensity distribution in the axial $I(z,t)$ and radial $I(r,t)$ direction for Re_i = 880. b) Radial profile and axial profile of light reflected intensity $\tilde{I} = I / I_{\max}$ taken at ξ = 0.5. (1) : vortex core, (2): inflow, (3): outflow.

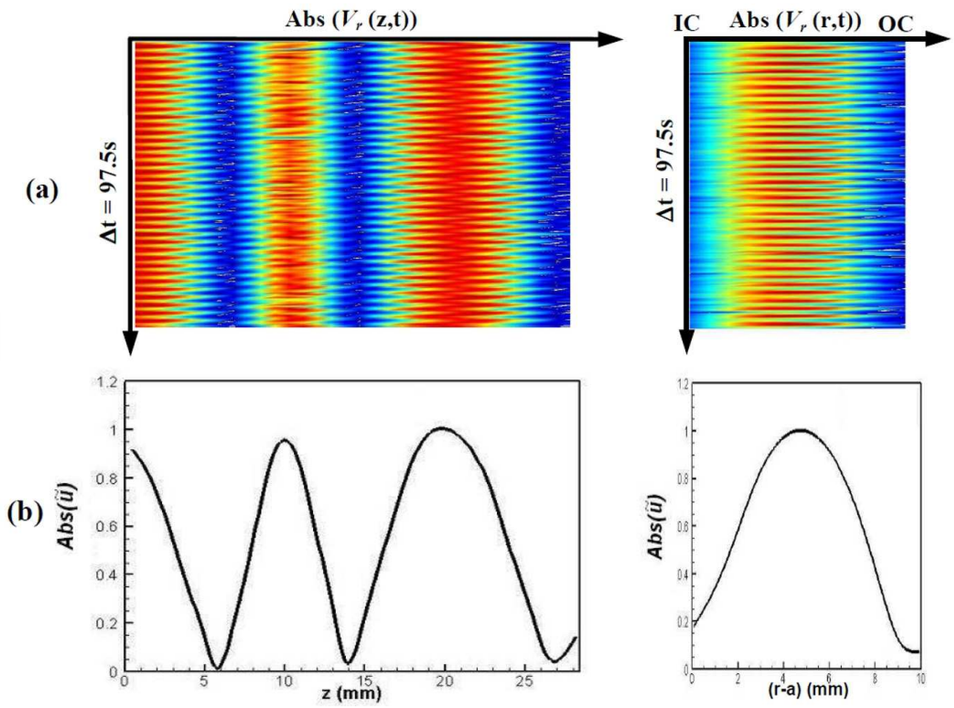

Fig. 18. a) Space-time diagrams of the absolute value of radial velocity component for Re_i = 880, b) Radial and axial profiles of the absolute value $\tilde{u} = V_r / V_{r\max}$ of the radial velocity component measured at ξ = 0.5.

so that the Brownian motion can be neglected. The comparison of the space-time diagrams obtained from flow visualization and PIV measurements performed for different flow regimes confirms that in the case of the fixed outer cylinder the reflective particles in the flow give information on the radial velocity component. Therefore, the commonly admitted conjecture that the reflective particles give information on the shear rate (Savas 1985) is in contradiction with the quantitative results. In fact, Fig. 19 shows profiles of different flow properties in the axial and radial direction. None of them has a similar behaviour as the reflected light intensity profile (Fig. 17b, 18b). These results give a more precise content on the fact the small anisotropic particles align with the flow streamlines (Savas 1985, Gauthier *et al*. 1998, Matisse *et al*. 1984) by giving the precision on the velocity component which bears these alignment.

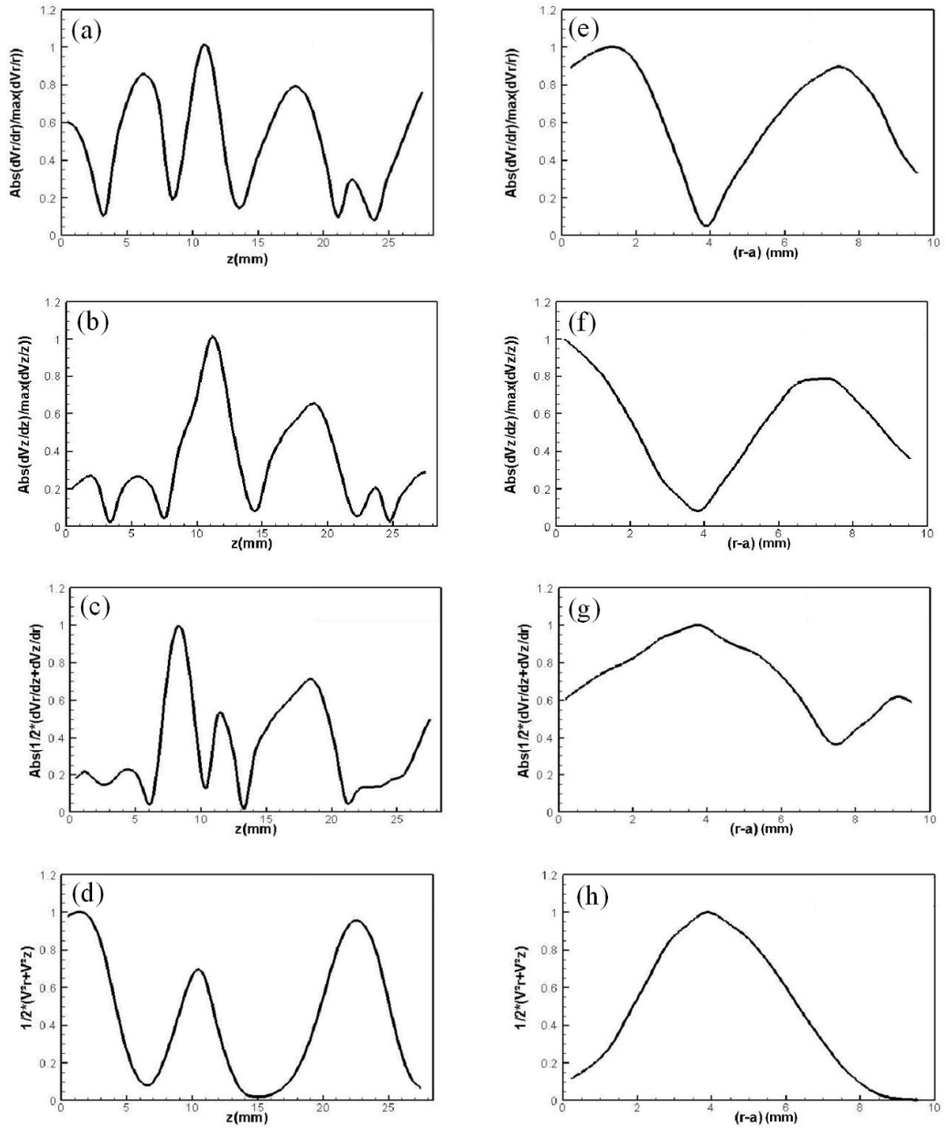

Fig. 19. Axial profiles of the absolute values of flow characteristics measured at ξ = 0.5: a) $\dot{\varepsilon}_{rr}$, b) $\dot{\varepsilon}_{zz}$, c) $\dot{\varepsilon}_{rz}$ and d) kinetic energy *E*; Radial profiles of the absolute values of flow characteristics measured in the outflow: e) $\dot{\varepsilon}_{rr}$, f) $\dot{\varepsilon}_{zz}$, g) $\dot{\varepsilon}_{rz}$ and h) kinetic energy *E*.

One should mention that our results were verified for TVF, WVF and MWVF in which the radial velocity component has a magnitude larger than that of the axial component. For turbulent Taylor vortex flow (TTVF), no conclusive observation has been made (Fig. 20). Following the results from (Gauthier et *al.* 1998) one would expect the applicability of the present results to pre-turbulent patterns observed in flow between differentially rotating discs (Cros *et al.* 2002).

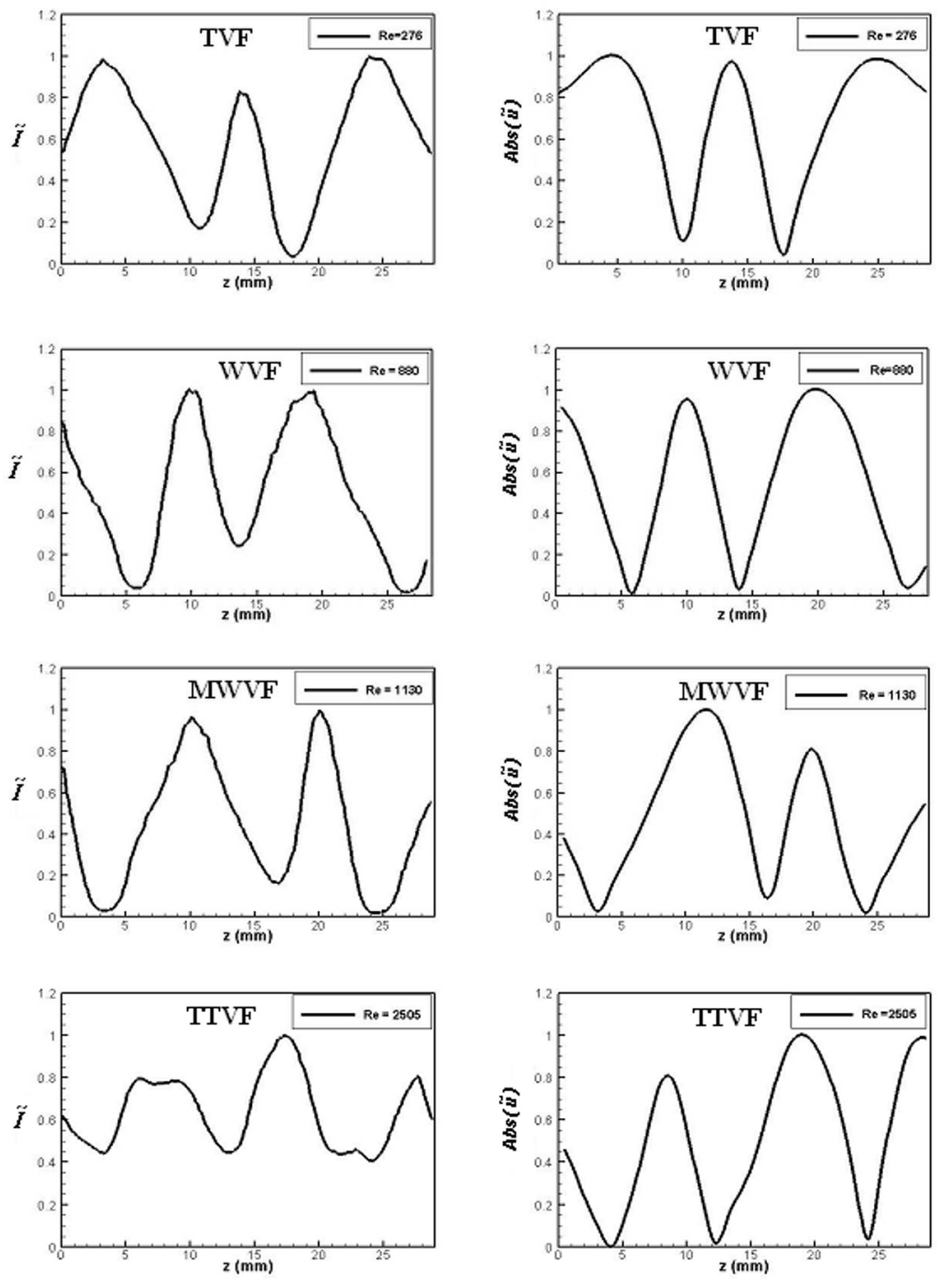

Fig. 20. Axial profiles of the absolute values of flow characteristics measured at $\xi = 0.5$ for different regimes TVF, WVF, MWVF and TTVF

6. Spatio-temporal structure of spiral vortex flow

6.1 PIV velocity measurements

The velocity and vorticity fields of the spiral vortex flow (SVF) for Re_o = -299 and Re_i = 212 in the radial-axial plane (*r*,*z*) of the flow are shown in Fig. 21. The measurement zone is located in the lower part of the system ($\zeta \in [14,17]$) from the bottom. The instantaneous velocity fields are regular and show very well the axial motion of the vortices.

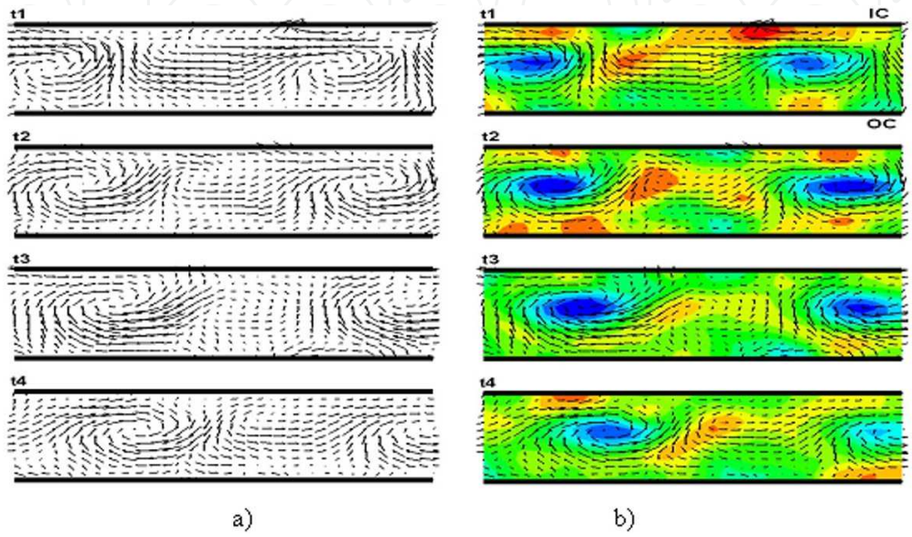

Fig. 21. The instantaneous velocity (arrows) and vorticity fields of the SVF for 4 records (t_{i+1} = t_i+0.5s). The color varies from blue (minimal negative vorticity) to red (maximal positive vorticity).

The space-time diagrams of velocity component $V_r(z,t)$ and $V_z(r,t)$ (Fig. 22c-d) confirmed the result from visualization using Kalliroscope flakes that the Taylor spiral vortex pattern is composed of a pair of vortices which propagate along and around the inner cylinder Fig. 22 a-b. Moreover it was revealed that the separatrix between two vortices in a spiral are inclined as in numerical simulations (Ezersky *et al.*, 2010). The radial velocity vanishes in the vortex core while its amplitude is maximal in the outflow and in the inflow. There exists an asymmetry between the inflow and outflow which is well pronounced for the spiral flow (Fig. 23a). In the radial direction, the axial velocity $w(\xi)$ is characterized by an asymmetry in the radial direction: it vanishes at $\xi \approx 0.39$ (Fig. 23d). Similarly the profile of the radial velocity $u(\xi)$ presents an asymmetry, and reaches a maximum around $\xi_0 \approx 0.4$, meaning that the spiral core is located in the region near the inner cylinder (Fig. 23b). The application of the Rayleigh circulation criterion for counter-rotating cylinders shows that the potentially unstable zone is located between ξ = 0 and the nodal surface $\xi_0 = \sqrt{\left(\eta^2 - \mu\right)/\left(1-\mu\right)}$, where $\mu = \eta \mathrm{Re}_o / \mathrm{Re}_i$. In our experiment with η = 0.8, ξ_0 = 0.38 for μ = - 1.13 and ξ_0 = 0.42 for μ = - 0.99. This indicates that the centrifugal instability in case of counter-rotating cylinders is penetrative instability (i.e. it invades the potentially stable zone near the outer cylinder). Using the formula (3-5), the meridional kinetic energy, the radial and axial elongations and the shear rate for the spiral vortex pattern have been computed (Fig. 24).

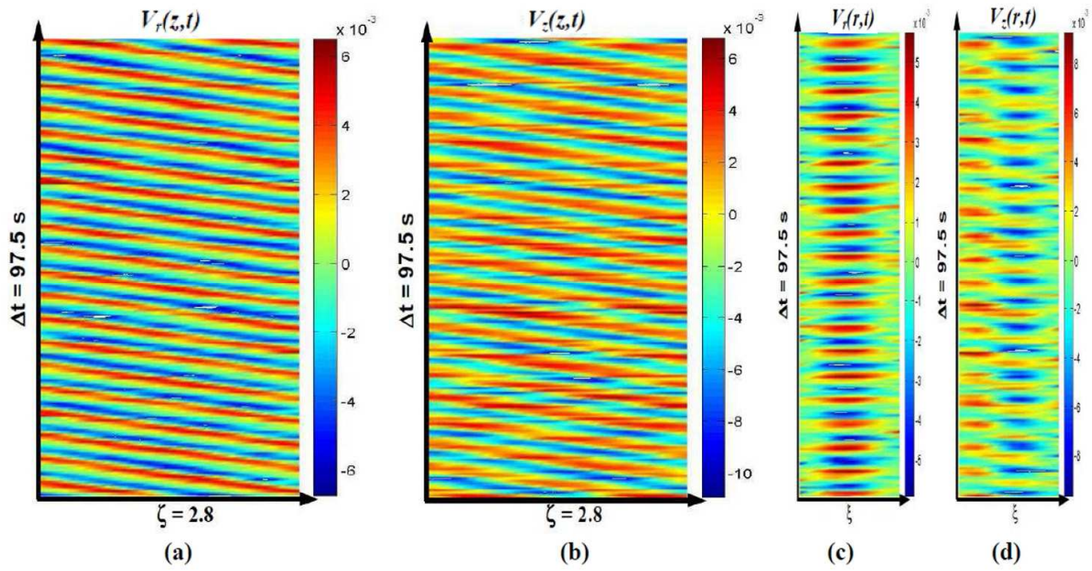

Fig. 22. Space-time diagrams of velocity components for Re_o = -299 and Re_i = 212 : a) $V_r(z,t)$, b) $V_z(z,t)$, c) $V_r(z,t)$, d) $V_z(x,t)$.

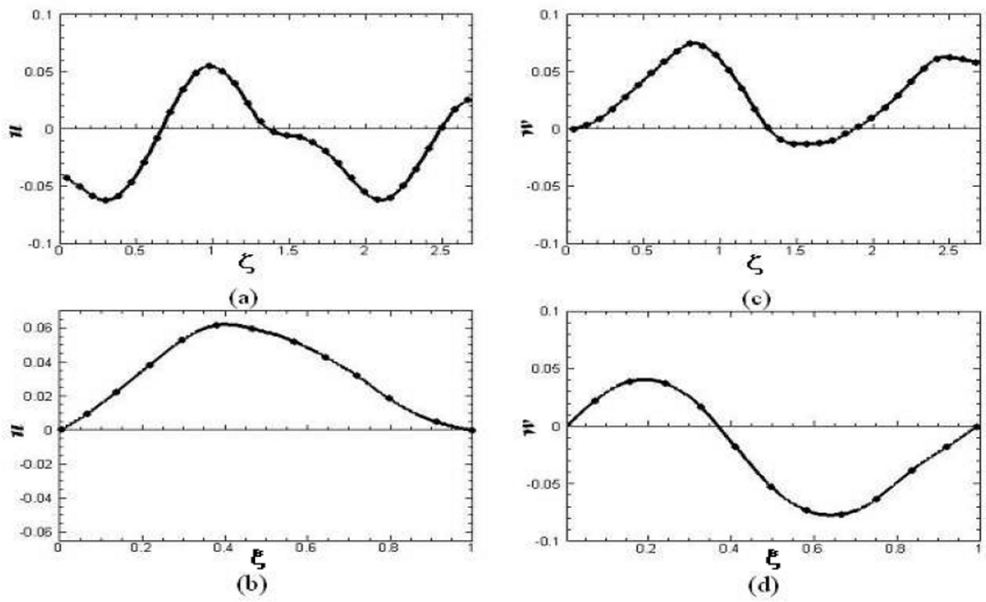

Fig. 23. Instantaneous velocity profiles u and w for Re_i=212, Re_o=-299. Axial variation of velocity component at the midgap (ξ = 0.5) : a) $u(\zeta)$ and c) $w(\zeta)$. Radial variation of velocity components: b) Radial component $u(\xi)$ at outflow, d) axial component $w(\xi)$ in the vortex core.

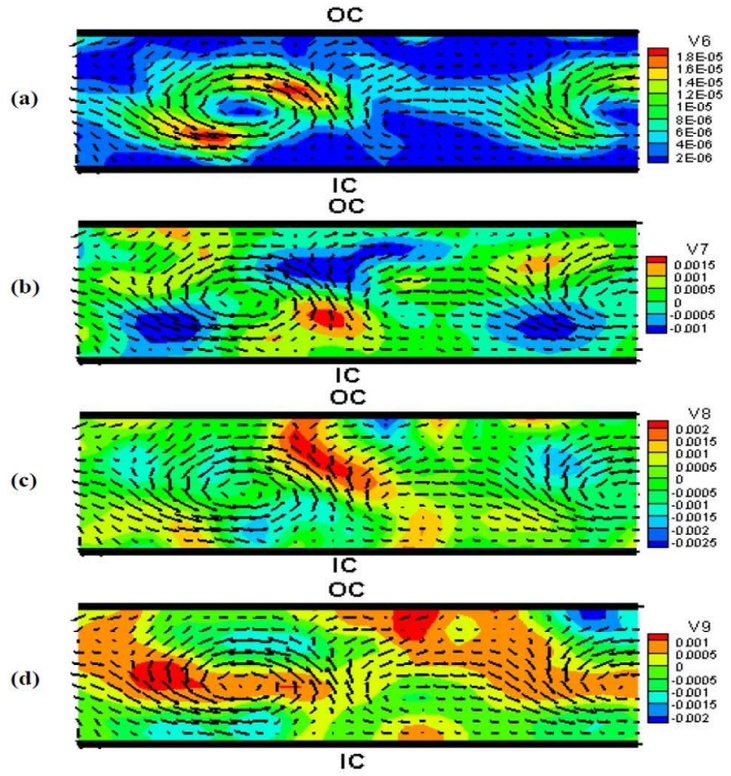

Fig. 24. Cross-section (r,z) of hydrodynamics fields for SVF : a) kinetic energy E; b) axial elongation $\dot{\varepsilon}_{zz}$ c) radial elongation $\dot{\varepsilon}_{rr}$ d) shear rate ε_{rz} .

6.2 Intensity of light reflected by Kalliroscope *vs*. velocity component

Comparison of the space-time diagrams, reveals a strong similarity between diagrams obtained by Kalliroscope flakes and those of the axial velocity component $V_z(z,t)$ and $V_z(r,t)$. Fig. 25a and Fig. 25b illustrate the time-average profiles in the axial and radial directions respectively of light reflected intensity and axial velocity component. Fig. 25c demonstrates discrepancies between radial velocity and intensity I for this case. The minima and maxima of intensity I are observed at approximately the same coordinates as minima and maxima of axial velocity V_z. It should be noted that the absolute value of the axial velocity vanishes in the vortex core while it reaches the maximum in the outflow and in the inflow. The reflected light intensity vanishes in the vortex core because of the weak motion of Kalliroscope flakes.

These plots highlight the fact that Kalliroscope particles give a signature of the axial velocity component measured in axial and radial direction.

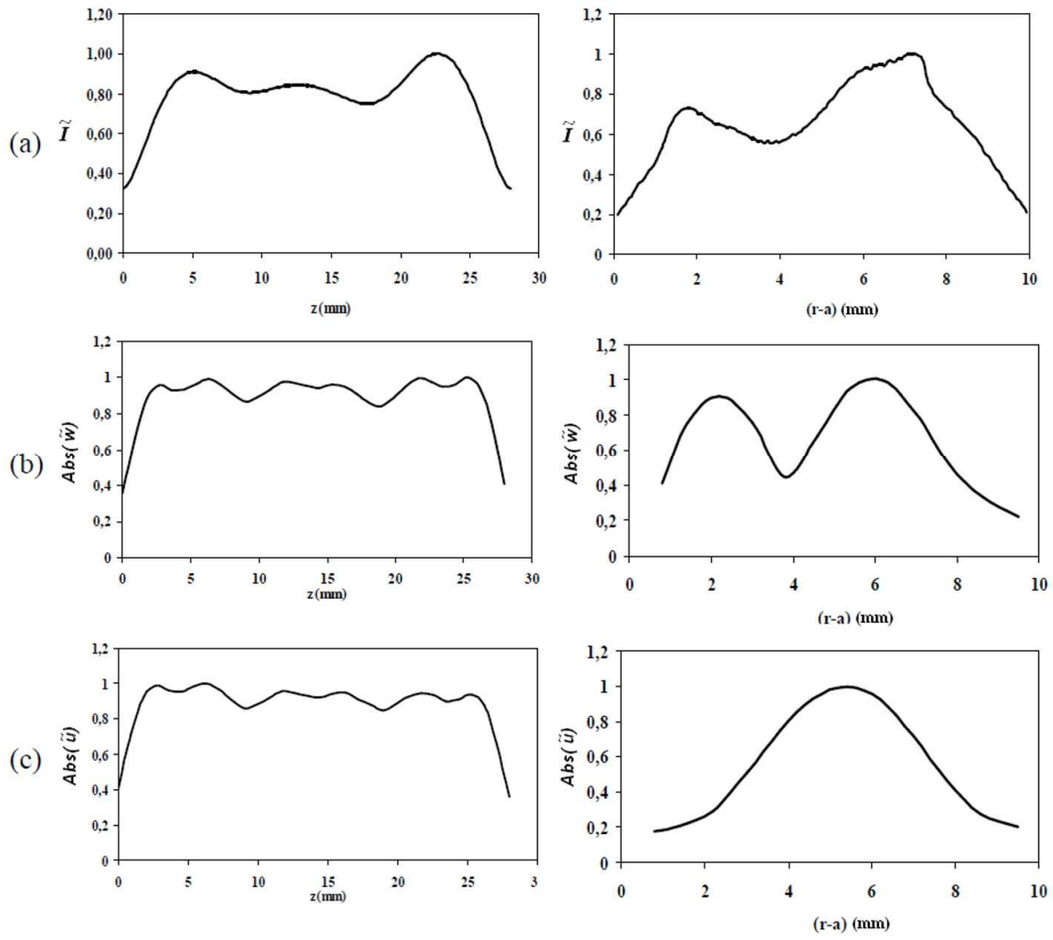

Fig. 25. a) Radial profile and axial profile of light reflected intensity $\tilde{I}$ taken at $\xi = 0.5$ b) Radial and axial profiles of the absolute value of the axial velocity component $\tilde{w} = V_z / V_{z\max}$ measured at $\xi = 0.5$; c) Radial and axial profiles of the absolute value $\tilde{u}$ of the radial velocity component measured at $\xi = 0.5$

6.3 The velocity field in the vicinity of defects

When the Reynolds number Re_i is increased , the pattern of the spiral vortex flow becomes unstable and spatio-temporal defects appear as a result of vortex merging (annihilation event) or of splitting of a vortex (creation event). The creation and annihilation events appear randomly in the pattern; they are due to long wavelength modulations. The velocity field was determined in the neighborhood of the spatio-temporal defects for Re_i = 227 and Re_o = -299. The defect was localized as point where amplitude of velocity field is closed to zero $V_z^2 + V_r^2 \approx 0$ and phase of the field has nonzero circulation around this point in the plane (z,t) (Fig. 26a-b black ellipses near t_d = 42s and z_d = 12 mm). A special attention was focused on the spatiotemporal behavior of radial and axial velocity components across the defect. Fig. 27a shows the temporal evolution of the axial and radial velocity components at the position of the defect and Fig. 27b shows the velocity profile taken at the collision time.

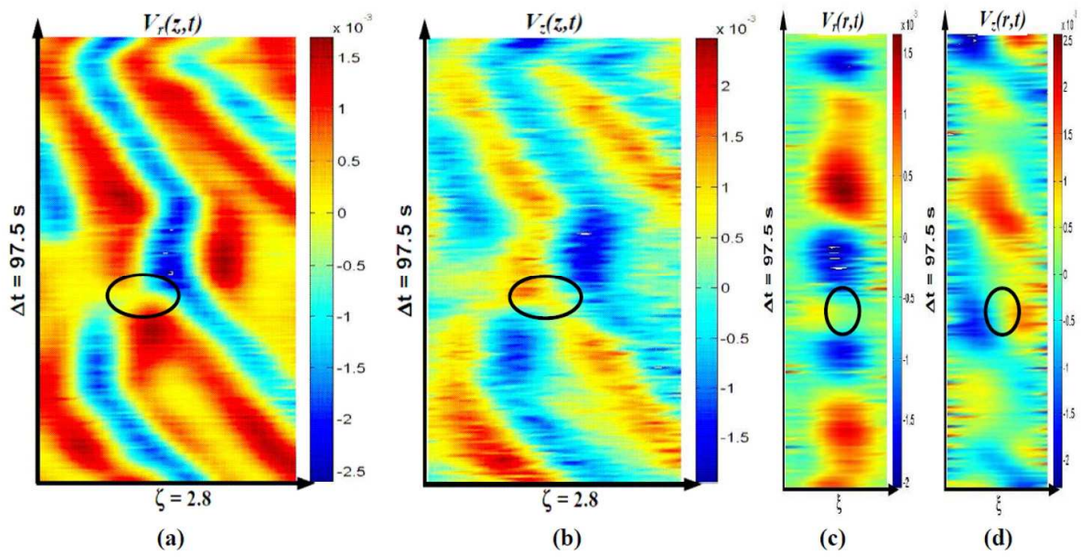

Fig. 26. Space-time diagrams of velocity components in the neighbourhood of the defect for Re_i=227 , Re_o=-299 : a) V_r(z,t) , b) V_z(z,t), c) V_r(r,t) and d) V_z(r,t).

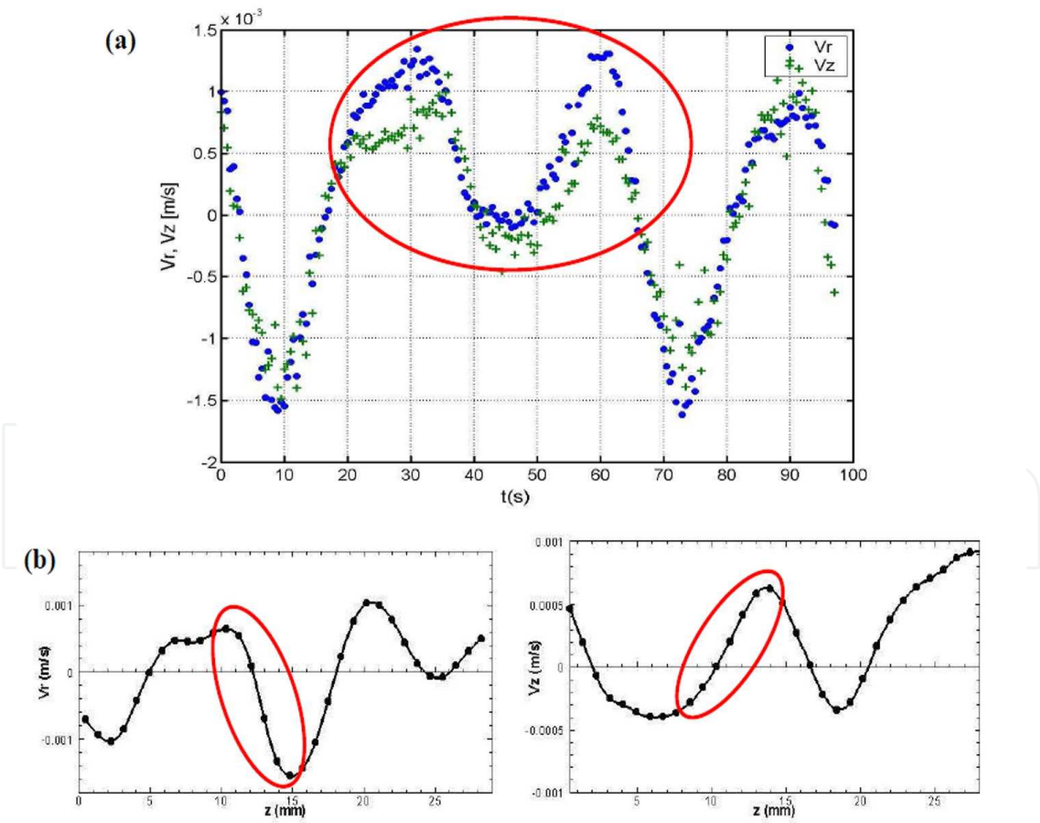

Fig. 27. Velocity profiles through the defect at the mid-gap (ξ = 0.5), for Re_i = 227 and Re_o = -299: a) The temporal evolution of radial and axial velocity components, b) Spatial evolution of radial and axial velocity components.

In the neighborhood of the defect, the temporal variation of both velocity components follows a parabolic law (Fig. 27a):

$$V_r(t) \approx \alpha(t - t_d)^2 \; ; \quad V_z(t) \approx \beta(t - t_d)^2 \tag{5}$$

while the spatial evolution is linear in the neighborhood of the defect (Fig. 27b):

$$V_r(z) \approx a(z - z_d) \quad ; \; V_z(z) \approx b(z - z_d) \tag{6}$$

The coefficients of the best fit are given in the Table. These results are in agreement with the solutions of the Ginzburg-Landau equation near a defect as was shown in Ezersky et *al.*, 2010.

Coefficient	α	β	a	b
Best fit value	0.01	0.07	-0.62	0.21

Table 1. Best fit coefficients of the temporal and spatial evolution of the velocity field in the neighbourhood of a defect.

7. Summary

This chapter has made a focus on the correspondence between the intensity of reflected light by particles and the velocity components in the meridional plane (*r*,*z*). When the outer cylinder is fixed, there is a correspondence between radial velocity component and the intensity of light reflected by anisotropic particles. This result has confirmed recent numerical simulations [Gauthier 1998]. When cylinders are counter-rotating, the intensity of light reflected by anisotropic particles is related to the axial velocity component. To investigate all the aspects of the transition to turbulence in closed or open flows, visualization by particle seeding and velocimetry techniques (LDV, UDV, PIV)are very complementary as they permit to access to different flow characteristics. In fact, the reflective flakes allow to access to flow properties on a large spatial extent and for a long time, and it is possible to evidence the spatio-temporal evolution to turbulence in each directions. For example the study of defects (sources, sinks, dislocations, ...) has facilitated the application of the Ginzburg-Landau model to the study of stationary and time-dependent patterns, the transition to chaos or weak turbulence has been characterized using results from visualization. The velocimetry techniques allow therefore to access to physical quantities needed in the model of turbulence (kinetic energy, rate of strain, vorticity, momentum,...) which are useful for validation of theoretical models for example in computing structure coefficients of the statistical distributions. The choice of appropriate technique depends on flow under consideration. In some cases, visualization by anisotropic particles is more preferable than LDV or PIV technique. Besides its simplicity and low cost, it is possible to visualise larger spatial extent, and to record long time data and therefore obtain a better power spectra. The problem of correlation of data obtained from anisotropic particles and velocimetry data is far from being solved, it represents a big challenge for experimental research in Hydrodynamics. Although some similarities between these two methods were found in the case of Couette-Taylor flow patterns, there are many fundamental questions that are far from being resolved:

1. How image brightness depends on particle concentration or particle orientation?
2. How concentration or orientation depends on velocity field characteristics?
3. Intensity of image brightness is a two dimensional field. How to project three dimensional field of particle concentration or orientation on two dimensional plane?

The answers to these questions will enable researchers in Hydrodynamics to understand spatio–temporal structures of closed flows by comparing results obtained from different techniques (velocimetry, visualization) and numerical simulations.

8. Acknowledgements

This work has been benefited from a financial support from the CPER-Haute-Normandie under the program THETE.

9. References

Abcha N.; Latrache N.; Dumouchel F. & Mutabazi I.(2008). Qualitative relation between reflected light intensity by Kalliroscope flakes and velocity field in the Couette-Taylor flow system, *Experiments in Fluids* Vol. 45, p.85.

Ahlers G.D.; Cannell D.S.; Dominguez-Lerma M.A.& Heinrichs R. (1986). Wavenumber selection and Eckhaus instability in Couette-Taylor flow, *Physica D* Vol. 23, p.202.

Andereck C. D.; Liu S.S. & Swinney H.L. (1986). Flow regimes in a circular Couette system with independently rotating cylinders, *Journal of Fluid Mechanics* Vol.164, p.155.

Bergé P., Pomeau Y. & Vidal Ch. (1984). L'ordre dans le chaos, Hermann, Paris.

Bot P. & Mutabazi I. (2000). Dynamics of spatio-temporal defects in the Taylor-Dean system, *European Physics Journal* B Vol. 13, p.141.

Chossat P. & Iooss G. (1994). *The Couette-Taylor Problem*, Applied Mathematical Science 102, Springer-Verlag, New-York.

Coles D. (1965). Transition in circular Couette flow, *Journal of Fluid Mechanics* Vol.21, p.385.

Cros A. & Le Gal P.(2002). Spatiotemporal intermittency in the torsional Couette flow between a rotating and a stationary disk, *Physics of Fluids* Vol.14, p.3755.

Cross M. C. & Hohenberg P. C. (1993). Pattern Formation Out of Equilibrium, *Review of Modern Physiscs* Vol. 65, p.851.

Demay Y. & Iooss G. (1984). Calcul des solutions bifurquées pour le problème de Couette-Taylor avec les deux cylindres en rotation, *Journal de Mécanique Théorique et Appliquée*, Numéro spécial p.193.

Dominguez-Lerma M.A.; Ahlers G. & Cannell D.S. (1985). Effects of Kalliroscope flow visualization particles on rotating Couette-Taylor flow, *Physics of Fluids* Vol. 28, p.1204.

Durst F. & Whitelaw J.H. (1976). *Principles and Practice of Laser-Doppler Anemometry*, Academic Press, New York.

Egbers Ch. & Pfister G. (eds) (2000). *Physics of Rotating Fluids*, Lectures Notes in Physics 549, Springer Berlin.

Ezersky A.B.; Abcha N. & Mutabazi I. (2010). The structure of spatio-temporal defects in a spiral pattern in the Couette-Taylor flow. *Physics Letters A* Vol.374, p. 3297.

Gauthier G., Gondret P. & Rabaud M. (1998). Motions of anisotropic particles : Application to visualization of three-dimensional flows, *Physics of Fluids* Vol. 10, p.2147.

Goharzadeh A. & Mutabazi I. (2010). Measurement of coefficients of the Ginzburg-Landau equation for patterns of Taylor spirals, *Physical Review E* Vol. 82, p.016306.

Hoffmann C.; Lücke M. & Pinter A. (2005). Spiral vortices traveling between two rotating defects in the Taylor-Couette system, *Physical Review E* Vol.72, p. 056311.

Jensen K. D. (2004). *Journal of the Brazilian Society of Mechanical Science & Engineering*, Vol. XXVI(4), p. 401.

Langford W. F.; Tagg R.; Kostelich E. J.; Swinney H. L. & Golubitsky M. (1988). Primary instabilities and bicriticality in flow between counter-rotating cylinders, *Physics of Fluids* Vol.31, p. 776.

Marcus P. S. (1984). Simulation of Taylor-Couette flow, Part 2: Numerical results for wavy-vortex flow with one travelling wave. *Journal of Fluid Mechanics* Vol. 146, p.65.

Matisse P. & Gorman M. (1984). Neutrally buoyant anisotropic particles for flow visualization, *Physics of Fluids* Vol.27, p.759.

Mutabazi I.; Wesfreid J.E. & Guyon E. (2006). *Dynamics of Spatio-Temporal Cellular Structures*, Springer, New York.

Peerhossaini H. & Wesfreid J.E. (1988). On the inner structure of streamwise Görtler vortices, *International Journal of Heat and Fluid Flow* Vol. 9, p. 12.

Provansal M.; Mathis C. & Boyer L. (1987). Bénard-von Karman instability: transient and forced regimes, *Journal of Fluid Mechanics* Vol. 182, p.1.

Savas Ö (1985). On flow visualization using reflective flakes, *Journal of Fluid Mechanics* Vol. 152, pp.235.

Takeda Y.; Fischer W.E. & Sakakibara J. (1994). Decomposition of the modulated waves in rotating Couette system, *Science* Vol. 263, p.502.

Taylor G.I. (1923). Stability of a viscous liquid contained between two rotating cylinders, *Philosophical Transactions of the Royal Society A* Vol. 223, p.289.

Thoroddsen ST; Bauer JM (1999). Qualitative flow visualization using colored lights and reflective flakes, *Phys. Fluids* Vol. 11, p.1702.

Van Dyke M. (1982). *An Album of Fluid Motion*, Parabolic, Stanford.

Wereley S.T. & Lueptow R.M. (1994). Azimuthal velocity in supercritical circular Couette flow. *Experiments in Fluids* Vol.18, pp.1.

Wereley S.T. & Lueptow R.M. (1998). Spatio-temporal character of non wavy and wavy Taylor-Couette flow, *Journal of Fluid Mechanics* Vol. 364, p.59.

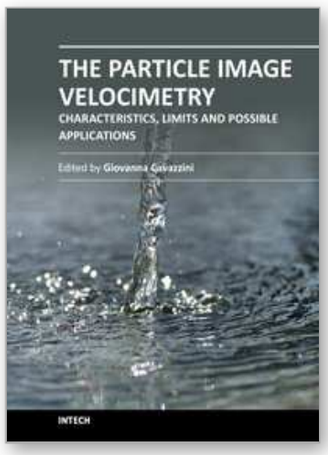

The Particle Image Velocimetry - Characteristics, Limits and Possible Applications

Edited by PhD. Giovanna Cavazzini

ISBN 978-953-51-0625-8
Hard cover, 386 pages
Publisher InTech
Published online 23, May, 2012
Published in print edition May, 2012

The Particle Image Velocimetry is undoubtedly one of the most important technique in Fluid-dynamics since it allows to obtain a direct and instantaneous visualization of the flow field in a non-intrusive way. This innovative technique spreads in a wide number of research fields, from aerodynamics to medicine, from biology to turbulence researches, from aerodynamics to combustion processes. The book is aimed at presenting the PIV technique and its wide range of possible applications so as to provide a reference for researchers who intended to exploit this innovative technique in their research fields. Several aspects and possible problems in the analysis of large- and micro-scale turbulent phenomena, two-phase flows and polymer melts, combustion processes and turbo-machinery flow fields, internal waves and river/ocean flows were considered.

InTech Europe
University Campus STeP Ri
Slavka Krautzeka 83/A
51000 Rijeka, Croatia
Phone: +385 (51) 770 447
Fax: +385 (51) 686 166
www.intechopen.com

InTech China
Unit 405, Office Block, Hotel Equatorial Shanghai
No.65, Yan An Road (West), Shanghai, 200040, China
中国上海市延安西路65号上海国际贵都大饭店办公楼405单元
Phone: +86-21-62489820
Fax: +86-21-62489821

IntechOpen